

Strengthening reactive metal-support interaction to stabilize high-density Pt single atoms on electron-deficient g-C₃N₄ for boosting photocatalytic H₂ production

P. Zhou, D. Su

To be published in "Nano Energy"

February 2019

Center for Functional Nanomaterials
Brookhaven National Laboratory

U.S. Department of Energy

USDOE Office of Science (SC), Advanced Scientific Computing Research (SC-21)

Notice: This manuscript has been authored by employees of Brookhaven Science Associates, LLC under Contract No. DE-SC0012704 with the U.S. Department of Energy. The publisher by accepting the manuscript for publication acknowledges that the United States Government retains a non-exclusive, paid-up, irrevocable, world-wide license to publish or reproduce the published form of this manuscript, or allow others to do so, for United States Government purposes.

DISCLAIMER

This report was prepared as an account of work sponsored by an agency of the United States Government. Neither the United States Government nor any agency thereof, nor any of their employees, nor any of their contractors, subcontractors, or their employees, makes any warranty, express or implied, or assumes any legal liability or responsibility for the accuracy, completeness, or any third party's use or the results of such use of any information, apparatus, product, or process disclosed, or represents that its use would not infringe privately owned rights. Reference herein to any specific commercial product, process, or service by trade name, trademark, manufacturer, or otherwise, does not necessarily constitute or imply its endorsement, recommendation, or favoring by the United States Government or any agency thereof or its contractors or subcontractors. The views and opinions of authors expressed herein do not necessarily state or reflect those of the United States Government or any agency thereof.

Strengthening Reactive Metal-Support Interaction to Stabilize High-Density Pt Single Atoms on Electron-deficient *g*-C₃N₄ for Boosting Photocatalytic H₂ Production

Peng Zhou,¹ Fan Lv,¹ Na Li,⁵ Yelong Zhang,¹ Zijie Mu,¹ Yonghua Tang,¹ Jianping Lai,¹ Yuguang Chao,¹ Mingchuan Luo,¹ Fei Lin,¹ Jinhui Zhou,¹ Dong Su⁵ and Shaojun Guo*^{1,2,3,4}

¹Department of Materials Science and Engineering, ²The Beijing Innovation Center for Engineering Science and Advanced Technology, ³Department of Energy and Resources Engineering, ⁴Key Laboratory of Theory and Technology of Advanced Batteries Materials, College of Engineering, Peking University, Beijing 100871, China, E-mail: guosj@pku.edu.cn.

⁵Center for Functional Nanomaterials, Brookhaven National Laboratory, Upton, NY 11973, USA.

Abstract: Tuning reactive metal-support interaction (RMSI) is a promising approach to optimizing catalytic active sites *via* the electronic, geometric and compositional effects. In general, the RMSI is conducted on the reducible oxides *via* a high-temperature reaction (> 550 °C). Herein we report a strong RMSI between Pt single atom (PtSA) and non-oxide-based *g*-C₃N₄ built by an *in-situ* photocatalytic reduction method at a sub-zero temperature. The experimental observation confirms that the rich N vacancies in *g*-C₃N₄ produce an obvious electron-deficient effect, which greatly enhances the RMSI. This strong RMSI contributes to the highest PtSA coverage density of 0.35 mg m⁻² reported to date in carbon-based materials and outstanding H₂-evolution activity of 174.5 mmol g⁻¹ h⁻¹ *per* PtSA relative to those on the electron-rich *g*-C₃N₄. The structure simulation reveals that the RMSI can not only stabilize the PtSA on the electron-deficient *g*-C₃N₄ *via* the strong chemical bond between PtSA and the two-coordinated C (C_{2C}) sites caused by the N vacancies, but also promises the PtSA with an optimized electronic and geometric structures for capturing photogenerated electrons and producing H₂. This finding opens a new channel for designing and manipulating single atom-loaded photocatalyst *via* the RMSI at a sub-zero low temperature.

Keywords: RMSI; PtSA; *g*-C₃N₄; N vacancy; H₂ production

1. Introduction

The single atom (SA) catalyst with unique physicochemical property is a new class of catalytic material system for boosting the catalysis.[1-5] Designing the high coverage density of SAs is definitely an effective strategy for improving the utilization efficiency of noble metal catalyst. However, in all the established solution-chemistry methods, controlling the metal single atoms (SAs) with high coverage density on the catalyst surface is extremely difficult to be achieved due to the undesirable nucleation growth and poor stability.[6] Although some ligand molecules have recently been additionally introduced to stabilize the noble metal SAs, the as-made noble metal SAs easily aggregate due to the removing of ligand molecules in the catalytic reactions.[7-9] Besides the demand for the high coverage density and stability, the high-performance SAs on catalysts should also satisfy the electronic and geometric requirements, which strongly depends on the chemical state of support.[10-13]

Recently, a reactive metal-support interaction (RMSI) provides a new strategy to optimize catalytic active sites *via* the electronic, geometric and compositional effects.[14,15] In general, the RMSI is completed by a well-designed chemical reaction between the metal and the reducible oxide supports at a high reduction temperature (> 550 °C),[16] which undesirably limits the composition and morphology varieties of catalysts. Especially for noble metal SAs-loaded catalyst, the high preparation temperature easily leads to the aggregation of noble metal SAs.[17] Some reactive non-oxide-based two-dimensional supports, such as *g*-C₃N₄ and carbides, receive little attention. Those supports often contain numerous unsaturated atoms and own a wide-adjusted structure, which provides a potential opportunity to build a strong RMSI between SAs and carbides at a low temperature.[17-19] Regardless, the RMSI between SAs and non-oxide-based support is not clear even though it is key to guiding the design of SAs-loaded catalyst.

Herein, we report a strong RMSI between PtSA and an electron-deficient *g*-C₃N₄ *via* an *in-situ* photocatalytic reduction method at a sub-zero temperature. The X-ray absorption near edge structure (XANES) and high-angle annular dark field-scanning transmission electron microscopy (HAADF-STEM) results confirm that the surface of *g*-C₃N₄ is covered with high-density PtSAs. The X-ray photoelectron spectroscopy (XPS) and electron spin resonance (ESR) indicate that the formation of rich N vacancies induces a distinct electron-deficient effect in *g*-C₃N₄, which greatly enhances the RMSI. The photocatalytic H₂-production test shows that the enhanced RMSI contributes to the improved catalytic activity of PtSAs-loaded *g*-C₃N₄. The density functional theory (DFT) simulations reveal that the RMSI can not only stabilize the PtSAs by the two-coordinated C (C_{2C}) atoms in the N vacancies of *g*-C₃N₄, but also optimize the electronic and geometric structures of

PtSAs for capturing electron and producing H₂. This work demonstrates that the RMSI can be achieved on supports other than oxides at an extremely low temperature (< 0 °C) while retaining the stability of the PtSAs.

2. Experimental and theoretical section

Chemicals. All of the reagents were of analytical grade, and used without further purification. H₂PtCl₆, dicyandiamide and triethanolamine were purchased from Aladdin (Shanghai, China). Deionized (DI) water was used in all experiments.

Synthesis of *g*-C₃N₄. *g*-C₃N₄ photocatalysts were prepared by following a typical thermal polymerization procedure.[20] Briefly, 5 g of dicyandiamide was put into a covered crucible, heated to 500 °C at a ramp rate of 2 °C min⁻¹ in a tube furnace under air condition and then maintained at this temperature for additional 4 h. After being cooled down to room temperature, the resultant powders were grinded and collected.

Synthesis of N-vacancy-riched *g*-C₃N₄. 1 g of *g*-C₃N₄ was put into a crucible, heated to 400, 560 and 620 °C at a ramp rate of 5 °C min⁻¹ in a tube furnace under N₂ condition, respectively, and maintained at the corresponding temperature for 2 h. After being cooled down to room temperature, the resultant powders were collected, noted as CN400, CN560 and CN620, respectively.

Synthesis of PtSA-loaded *g*-C₃N₄ (PtSA-CN). 20 mg of CN was dispersed in 10 mL of deionized water containing 4 μmol H₂PtCl₆ under magnetic stirring for 30 min. Next, the mixed solution was ultrasonicated for 30 min, and stirred for 12 h. Then, the mixed solution was rapidly frozen by liquid nitrogen, followed by irradiating under a 300 W Xe light with the light filter of 420 nm and IR. After 3 min irradiation, the ice layer was naturally melted. The formed solution was centrifugalized and separated. The obtained precipitates were further washed with deionized water for two times. Finally, the precipitates were dried in an oven at 60 °C for 12 h.

Synthesis of PtNP-loaded *g*-C₃N₄ (PtNP-CN). For a comparison, PtNP-loaded C₃N₄ was synthesized by directly irradiating the mixed solution of CN620 and H₂PtCl₆ without the pretreatment of liquid nitrogen. Other procedures were similar to the above preparation method for making the PtSA-loaded C₃N₄.

Catalyst characterization. The X-ray diffraction (XRD) patterns, obtained on an X-ray diffractometer (Rigaku, Japan) using Cu Kα radiation at a scan rate of 0.05° 2θ s⁻¹, were used

to characterize the crystalline phase of the samples. The accelerating voltage and applied current were 40 kV and 80 mA, respectively. The Brunauer-Emmett-Teller (BET) specific surface area (S_{BET}) of the samples was measured in a nitrogen adsorption apparatus (Micromeritics ASAP 2020, USA). Before nitrogen adsorption measurements, all the samples were degassed at 200 °C. The S_{BET} was determined by a multipoint BET method using adsorption data in the relative pressure (P/P_0) range of 0.05-0.3. The pore-size distributions were determined by the nitrogen adsorption volume *via* the Barret-Joyner-Halender (BJH) method assuming a cylindrical pore model. Aberration-corrected HAADF-STEM analysis was conducted on JEM-ARM200F transmission electron microscope with an accelerating voltage of 300 kV. X-ray photoelectron spectroscopy (XPS) measurements were performed on an ESCALAB 250Xi electron spectrometer with Mg K α (1253.6 eV) source. All binding energies were referenced to the C 1s peaks at 284.8 eV from the adventitious carbon. Electron spin resonance (ESR) experiments were conducted on an ER-200D spectrometer (Bruker, Germany) at a microwave frequency of 9.5 GHz under room temperature. The content of Pt elements in the as-prepared samples was analyzed by an inductively coupled plasma-atomic emission spectrometer (ICP-AES) on PerkinElmer Optima 7300DV. Steady-state and time-resolved photoluminescence emission spectra (332 nm excitation) were collected on a fluorescence spectrophotometer (Edinburgh Instruments, FLSP-920) at room temperature.

XAFS measurement and data analysis. XAFS spectra at the Pt L₃-edge were measured at the 1W1B beamline of Beijing Synchrotron Radiation Facility (BSRF), China. The storage ring of BSRF was working at the energy of 2.5 GeV with a maximum electron current of 250 mA. The hard X-ray was monochromatized with Si(111) double-crystal monochromator, and the detuning was done by 30% to remove harmonics. The acquired EXAFS data were processed according to the standard procedures using the ATHENA module of the IFEFFIT software packages. The k^3 -weighted $\chi(k)$ data in the k -space ranging from 2.0-11.5 Å⁻¹ were Fourier transformed to real (R) space using a hanning windows ($dk = 1.0$ Å⁻¹) to separate the EXAFS contributions from different coordination shells. To obtain the detailed structural parameters around Pt atom in the as-prepared samples, the quantitative curve-fittings were carried out for the Fourier transformed $k^3\chi(k)$ in the R-space using the ARTEMIS module of IFEFFIT3. Effective backscattering amplitudes $F(k)$ and phase shifts $\Phi(k)$ of all fitting paths were calculated by the *ab initio* code FEFF8.0. During the fitting analysis, the amplitude reduction factor S_0^2 was fixed to the best-fit value of 0.70, which was determined from fitting the reference sample of metal Pt bulk, PtN₂ bulk and PtCl₄ bulk. In general, it was difficult to

distinguish Pt-O, Pt-C and Pt-N coordination. Thus the Pt-O coordination was used to describe the Pt-C/N/O coordination. To fit the data of PtSA-CN400, PtSA-CN560, PtSA-CN620 and PtNP-CN620 samples, the interatomic distance (R) and the Debye-Waller factor (σ^2) were allowed to vary. We have distinguished Pt-C/N/O and Pt-Cl from Pt-Pt coordination, considering the existing bonding length difference between them.

Catalytic activity measurements. The photocatalytic H₂ production measurements were conducted in a double layered Pyrex vessel (inner volume of 200 mL with diameter of 50 mm and height of 100 mm). A 300 W Xe lamp with the light filters of 420 nm and IR was used as the light source. The focused intensity on the flask was $\sim 100 \text{ mW}\cdot\text{cm}^{-2}$, measured by a FZ-A visible-light radiometer (made in the photoelectric instrument factory of Beijing Normal University, China) with a wavelength range of 400-1000 nm. In a typical photocatalytic H₂ production experiment, 20 mg of the as-prepared photocatalyst was suspended in 100 mL of 10 vol% triethanolamine aqueous solution, and then bubbled with Ar through the reactor for 30 min to completely remove the dissolved oxygen. The suspension solution in the reactor was continuously stirred by a magnetic stirrer during the experiment. A thermostatic digital controller (HX-205) was used to control the temperature of reactor (25 °C). The amount of produced H₂ was tested every hour. 1 mL of gas sample was sampled from the headspace of the flask through the septum and analyzed by gas chromatography (GC-7890B, Agilent, America, TCD, with Ar as a carrier gas and 5 Å molecular sieve column). The obtained H₂ content was used to evaluate the H₂ production activity of different samples. The apparent quantum efficiency (AQE) measurements were performed under the irradiation of a 420 nm LED light with an irradiation density of 50 mW cm^{-2} . Others were same with the experiments above. The AQY of photocatalytic H₂ production was calculated by the equation (1):

$$\text{AQY} = 2 \times n(\text{H}_2)/n(\text{photons}) \times 100 \quad (1)$$

Where $n(\text{H}_2)$ and $n(\text{photons})$ denote the number of produced H₂ molecules and the number of incident photons, respectively.

Theoretical simulation. The geometry structures and electronic properties of PtSA-loaded *g*-C₃N₄ were investigated by the density functional theory (DFT) calculations based on the VASP package using the PBE exchange-correlation function.[21,22] The interaction between valence electrons and the ionic core was described by the PAW pseudo-potential. The model of *g*-C₃N₄ was simulated by a periodic atomic layer containing 96 C atoms and 128 N atoms. The N vacancy was built by removing a N_{2C} atom. The geometry structures of pure and N-

vacancy-riched $g\text{-C}_3\text{N}_4$ were optimized with the cutoff of 400 eV. All the atoms in the model were allowed to adjust until the magnitude of all residual forces was less than $0.001 \text{ eV \AA}^{-1}$. Considering the calculation cost, the geometry optimization was only performed at Gamma point. After the geometry optimization, the PDOS was calculated by the cutoff energy of 400 eV and the Monkhorst-Pack k-point mesh of $2 \times 2 \times 1$. The adsorptions of PtSAs at the low-coordinated $\text{C}_{2\text{C}}$ and $\text{N}_{2\text{C}}$ sites were considered. For a comparison, the PtNP was simulated by a Pt cluster containing 38 Pt atoms.

The adsorption energy (E_{ads}) of PtSA at the $\text{C}_{2\text{C}}$ and $\text{N}_{2\text{C}}$ sites was used to evaluate the stability of coordination structure, which was calculated by the following formula:

$$E_{\text{ads}} = E_{\text{CN+PtSA}} - E_{\text{CN}} - E_{\text{PtSA}} \quad (2)$$

where $E_{\text{CN+PtSA}}$ was the total free energy of PtSA-CN, E_{CN} was the free energy of CN and E_{PtSA} was the free energy of one PtSA in vacuum.

The E_{ads} of H^+ ion on the PtSA or PtNP was used to evaluate the H-reduction ability, which was calculated by the following formula:

$$E_{\text{ads}} = E_{\text{CN+PtSA+2H}} - E_{\text{CN+PtSA}} - 2E_{\text{H}} \quad (3)$$

where $E_{\text{CN+PtSA+2H}}$ was the total free energy of H-adsorbed PtSA-CN and E_{H} was the free energy of one H^+ ion in the H_3O^+ .

The desorption energy (E_{des}) of H_2 on the PtSA or PtNP was used to evaluate the H_2 -evolution ability, which was calculated by the following formula:

$$E_{\text{des}} = E_{\text{CN+PtSA}} + E_{\text{H}_2} - E_{\text{CN+PtSA+2H}} \quad (4)$$

where E_{H_2} was the free energy of one H_2 molecule in vacuum.

The electronic properties of PtSA-CN and PtNP-CN were also investigated by calculating the PDOS plots, which were performed with the cutoff energy of 400 eV and the Monkhorst-Pack k-point mesh of $2 \times 2 \times 1$. The photogenerated electron transfer between PtSA/PtNP and CN was constructed by calculating the charge density differences ($\rho_{\text{difference}}(\mathbf{r})$) of the PtSA-CN/PtNP-CN model after and before charging with two electrons:

$$\rho_{\text{difference}}(\mathbf{r}) = \rho_{\text{PtSA-CN+2e}}(\mathbf{r}) - \rho_{\text{PtSA-CN}}(\mathbf{r})$$

where $\rho_{\text{PtSA-CN+2e}}(\mathbf{r})$ and $\rho_{\text{PtSA-CN}}(\mathbf{r})$ were the charge density of PtSA-CN/PtNP-CN after and before charging, respectively.

3. Results and discussion

Firstly, the pure g - C_3N_4 was synthesized by annealing dicyandiamide at 500 °C in air.[23,24] Then, the g - C_3N_4 with different content of N vacancies was further treated at 400, 560 and 620 °C in N_2 , respectively. The corresponding products were noted as CN400, CN560 and CN620, respectively. X-ray diffraction (XRD) patterns of the CN400, CN560 and CN620 show a diffraction peak at 27.2° (**Fig. 1a**), indexed to the typical g - C_3N_4 as reported previously.[23,24] Besides, the intensity of diffraction peak at 27.2° decreases with increasing the treatment temperature, implying the weakening of crystallinity and production of defects. The electron spin resonance (ESR) was used to analyze the defect state of different CN. A stronger G factor at 3482 is observed in CN620 (**Fig. 1b**), belonging to N vacancy.[25] This indicates the existence of numerous defects, consistent with the XRD results. The UV-vis diffuse reflectance spectra (DRS) reveal that a progressive redshift in the absorption edge is achieved from CN400 to CN620 (**Fig. 1c**). The bandgaps of the different CN determined from the transformed Kubelka-Munk function progressively narrow from 2.62 eV for CN400, 2.47 eV for CN560 and 2.14 eV for CN620 (**Fig. 1d**). This redshift results from the formation of N vacancies. It is well known that in the structure of g - C_3N_4 , the C atoms are coordinated with three N atoms, while some N atoms are only coordinated with two C atoms (**Fig. S1a**). Those two-coordinated N atoms (N_{2C}) with low thermodynamic stability prefer to be desorbed rather than the three-coordinated N (N_{3C}) atom (**Fig. S2**). As a result, some N_{2C} vacancies were left (**Fig. S1b**). Meanwhile, two neighbor two-coordinated C atoms (C_{2C}) were formed.

Besides, the C_{2C} atoms easily produce a gap state according to the calculated projected density of state (PDOS) plots (**Fig. S1c**), which well explains the above redshift in DRS results. It should be noted that the gap state is nearly higher than the Fermi level (**Fig. S1c-3**), suggesting that the two C_{2C} atoms are electron-deficient. As a result, the C_{2C} atoms can act as an electron traps, which prefer to capture the photogenerated electrons rather than three-coordinated C (C_{3C}) or N (N_{3C}) atoms. Hence, the C_{2C} sites are the potential photocatalytic reducing centers. In contrast, the 2p states of N_{2C} atoms are mainly localized in the top of valence band. In the photocatalytic reaction, more holes are easily aggregated in the N_{2C} atoms.

The PtSA-loaded CN400, CN560 and CN620 (noted as PtSA-CN400, PtSA-CN560 and PtSA-CN620) were prepared by the method illustrated in **Scheme 1**. g - C_3N_4 photocatalyst and Pt precursor (H_2PtCl_6) were mixed in deionized water, and then rapidly frozen in the liquid nitrogen to form an ice bulk. On the g - C_3N_4 surface, the C_{2C} site was positively charged according to the above structure simulation. Hence, the negatively charged $[PtCl_6]^{2-}$ ion tended to be selectively adsorbed at the C_{2C} site. A 300 W Xe lamp with the light filter of 420 nm and IR was used as the light source to excite g - C_3N_4 in ice bulk, which produced the photogenerated electrons. The photogenerated electrons could reduce the surface adsorbed $[PtCl_6]^{2-}$ ion into the metal Pt species by the light irradiation of only 3

min. Especially, those C_{2C} sites with empty band-gap states preferred to receive the photogenerated electron from the valence band rather than the N_{3C} and C_{3C} sites. Hence, the $[PtCl_6]^{2-}$ ion trapped at the C_{2C} site was easier to be reduced compared with those adsorbed at other sites. It should be noted that those free $[PtCl_6]^{2-}$ ions delocalized in the ice bulk could not be reduced because the photogenerated electrons were difficult to be diffused into the ice layer. Besides, those free $[PtCl_6]^{2-}$ ions could also not be directly reduced by the light (> 420 nm) due to its low energy. As a result, only the $[PtCl_6]^{2-}$ ions adsorbed at the C_{2C} sites of $g-C_3N_4$ were selectively reduced. This method can not only effectively inhibit the undesirable growth of metal Pt species, but also selectively reduce Pt precursor at the N vacancy. As a comparison, the mixed solution of CN620 and Pt precursor was directly irradiated without the icing treatment. The obtained sample was noted as PtNP-CN620. According to the ICP-OES measurements, the Pt contents in PtSA-CN400, PtSA-CN560, PtSA-CN620 and PtNP-CN620 are 2.30, 1.45, 1.72 and 3.45wt%, respectively (**Table S1**).

The as-made samples were characterized by the aberration-corrected HAADF-STEM. The supra-high-density PtSAs are coated on the whole CN surface (**Fig. 2**). Especially, on the CN620 surface, the PtSAs shows an outstanding dispersion, and less aggregations of PtSAs are observed (**Fig. 2c and 2d**). It is speculated that the numerous N vacancies in CN620 can stabilize the PtSAs. This is further confirmed by the calculated adsorption energy (E_{ads}) of PtSA at the C_{2C} (N vacancy) and N_{2C} sites (**Fig. 2e and 2f**). The E_{ads} of PtSA at the C_{2C} site is more negative than that at the N_{2C} site, indicating that the PtSA prefers to be trapped at the C_{2C} site from the viewpoint of thermodynamics. Thus it is not strange that less aggregation occurs on CN620 surface with more C_{2C} sites. This implies that a strong RMSI probably exist between PtSA and CN620. Further, combining with the above theoretical simulation on the electronic properties of C_{2C} site, it can be speculated that the C_{2C} sites in CN act as the main centers for adsorbing, reducing and stabilizing the PtSAs. As another comparison, numerous PtNPs with the diameter ranging from 2 nm to 5 nm were prepared in the PtNP-CN620 without icing assistance (**Fig. S3**).

X-ray absorption fine structure (XAFS) measurements were carried out to further investigate the coordination structure of Pt species at atomic level. **Fig. 3a** shows the Pt L_3 -edge X-ray absorption near-edge structure (XANES) spectra of PtSA-CN400, PtSA-CN560, PtSA-CN620 and PtNP-CN620. The absorption edges of PtSA-CN400, PtSA-CN560 and PtSA-CN620 are higher than that of PtNP-CN620 or Pt foil. The Fourier-transformed (FT) k^3 -weighted extended X-ray absorption fine structure (EXAFS) spectra reveal that one main peak at 1.58 Å is observed in PtSA-CN400, PtSA-CN560 and PtSA-CN620 (**Fig. 3b**), corresponding to the first coordination shell of Pt.[13,26] To obtain the quantitative chemical configuration of Pt atom, the EXAFS fitting was also performed to extract the structure parameters (**Fig. S4**). The centered Pt atoms own three coordinating interactions:

Pt-C/N/O, Pt-Cl and Pt-Pt (**Table S2**). It should be noted that it is commonly difficult to distinguish the Pt-C, Pt-N and Pt-O coordination. In PtSA-CN400, PtSA-CN560 and PtSA-CN620, the coordination numbers of Pt-C/N/O and Pt-Cl approximate to 5 and 1, respectively. The mean bond lengths of Pt-C/N/O and Pt-Cl approximate to 2.03 and 2.29 Å, respectively. Considering the structure feature of CN, the PtSAs can be coordinated with two C_{2C} and one N_{2C} atoms or three N_{2C} atoms. The other three coordinating bonds can be attributed to two Pt-O bonds and one Pt-Cl bond. This reveals the reactive interaction between PtSAs and CN. It should be noted that those oxidizing bonds (Pt-O and Pt-Cl) are easily removed by the reducing H species in the photocatalytic H₂-production reaction.[27,28] In PtNP-CN620, a remarkable peak at 2.65 Å is observed, attributed to the Pt-Pt bond in the metal PtNP. This suggests that the PtNPs have a higher content in PtNP-CN620. The wavelet transform (WT) is used to analyze Pt L₃-edge EXAFS oscillations (**Fig. 3c and S5**). The WT maximum at 5.61 Å⁻¹ in PtSA-CN400, PtSA-CN560 and PtSA-CN620 could be assigned to the Pt-C/N/O bonding, also confirming the existence of PtSA.

The X-ray photoelectron spectroscopy (XPS) was used to analyze the chemical state of surface atoms. In the C 1s spectrum, a dominant C 1s peak at 288.4 eV corresponds to the three-coordinated C_{3C} groups (**Fig. 3d and S6a**) [23]. A weak peak at the high binding energy 289.6 eV is attributed to the C_{2C} at the N vacancy because the C_{2C} is electron-defected according to the above DFT calculation. With increasing the content of N vacancies, the peak at 289.6 eV is gradually enhanced, consistent with the above experimental results. The spectrum of N 1s contains a peak at 398.9 eV (**Fig. 3e and S6b**), corresponding to the N_{2C} in C-N-C groups [23,24]. However, the peak at 400.1 eV in PtSA-CN400 is improved to 400.6 eV in PtSA-CN620 and PtNP-CN620, associated with the N_{3C} in N(C)3 groups. This variation is attributed to the decreased electron density caused by the formation of N vacancies. Importantly, this electron-deficient effect in CN further induces the change in the chemical state of PtSA. As a result, the Pt 4f peaks exhibit a remarkable positive shift in PtSA-CN620 (**Fig. 3f**). Especially, the XPS peaks of Pt 4f at 75.5 eV and 78.5 eV in PtSA-CN400 move to 76.2 eV and 78.7 eV in PtSA-CN620, respectively. It should be noted that the XPS peak of N_{3C} 1s in pure CN620 is more negative than that in PtSA-CN620, implying the electron transfer from CN620 to PtSA (**Fig. 3e and S6b**). This strongly confirms a strong electronic interaction between PtSA and CN620, indicating an enhanced RMSI in PtSA-CN620. Besides, it is also suggested that increasing the content of N vacancies in CN can significantly enhance the RMSI.

In general, this high coverage density of PtSA on g-C₃N₄ can greatly narrow the distance between PtSA and photogenerated electrons on the surface, which is significant for improving the utilization efficiency of photogenerated electrons. N₂ physisorption measurements were used to examine the specific surface area and pore structure of different samples. The isotherms of the PtSA-CN400,

PtSA-CN560 and PtSA-CN620 have the obvious hysteresis loops at high relative pressure between 0.8 and 1.0, defined as type-IV mesoporous solids according to the Brunauer-Emmett-Teller (BDDT) classification (**Fig. S7**). The BET specific surface areas (BET) determined for PtSA-CN400, PtSA-CN560 and PtSA-CN620 were 41.4, 38.1 and 49.7 m² g⁻¹, respectively. Based on the measured BET area, the average covering density of PtSA on CN620 is calculated to be 0.35 mg m⁻², larger than those reported in the literature (**Table S3**).^[5,9,26] This indicates the advantage of the RMSI in preparing the high-density PtSA-loaded photocatalyst.

The photocatalytic H₂ production activities of the PtSA-CN400, PtSA-CN560, PtSA-CN620 and PtSA-CN620 were measured in a double layered Pyrex vessel under irradiation of a 300 W Xe lamp with a 420 nm cutoff filter, and by using triethanolamine as the electron donor. The results show that PtSA-CN620 owns a higher H₂ production rate (3.02 mmol g⁻¹ h⁻¹) than the PtSA-CN400 or PtSA-CN560 with a weaker RMSI (**Fig. S8a**). Moreover, the calculated H₂ production mass activity (174.5 mmol g⁻¹ h⁻¹) of PtSA-CN620 is 8-fold higher than that (20.5 mmol g⁻¹ h⁻¹) of PtNP-CN620 (**Fig. 4a**). In order to exclude the factor of light response range, the apparent quantum efficiencies (AQE) of as-prepared samples were examined under a 420 nm LED light source, in which the PtSA-CN620 shows the highest AQE of 0.544% compared to other samples (**Fig. S8b**). Hence, the wider light response range induced by the rich N vacancies is not the main factor for the higher photocatalytic activity of PtSA-CN620 compared to other samples. Instead, it is suggested that the strong RMSI is responsible for the high H₂ production rate of PtSA-CN620. Furthermore, PtSA-CN620 can stably work for 16 h without obvious activity decrease (**Fig. 4b**). The HRTEM images of samples after reaction reveals show that some PtNPs appear in the PtSA-CN400 and PtSA-CN560 (**Fig. S9a and S9b**). Especially, more and larger PtNPs are observed in PtSA-CN400 with less N vacancies. However, no PtNP appeared in PtSA-CN620 (**Fig. S9c**), and the XANES spectra also support the stability of PtSAs in PtSA-CN620 (**Fig. S10**). This confirms that the PtSAs in PtSA-CN620 are not deactivated or aggregated in the photocatalytic H₂-production reaction. The high stability of PtSAs in PtSA-CN620 can be attributed to the strong RMSI constructed by the *in-situ* photocatalytic reduction method described above.

Despite of the high coverage density and stability, the electronic property, such as electron-captured and hydrogen-reduced abilities, is another factor in determining the H₂ production activity of PtSAs on *g*-C₃N₄. Considering the relationship between the electron-captured ability of cocatalyst and the charge-carrier separation efficiency of photocatalyst, the steady-state and time-resolved photoluminescence (PL) spectra was used to study the charge-carrier separation and transfer efficiency in the as-prepared samples. As shown in **Fig. 4c**, compared to PtSA-CN400 and PtSA-CN400, PtSA-CN620 shows a weaker steady-state PL peak at 515 nm. This suggests that the

photogenerated carrier in PtSA-CN620 owns a longer lifetime. Besides, the time-resolved PL reveals that a faster charge transfer occurs in PtSA-CN620 with an average carrier lifetime of 3.40 ns (**Fig. 4c**).^[29] This is attributed to the coexistence of PtSA and N vacancy, which can promote the charge-carrier separation and transfer efficiency via the RMSI. To further investigate the underlying H₂-production mechanism of PtSAs on *g*-C₃N₄ via RMSI, the electronic property and H₂-production feature of PtSA located at the C_{2C} and N_{2C} sites of one CN model were calculated by the density functional theory (DFT). A PtNP with 38 Pt atoms was also considered as the comparison. The calculated PDOS plots of above geometry structures suggest that the 5d and 6s states of PtSA in the C_{2C} site are almost lower than the Fermi level (**Fig. 5a and 5b**). However, the partial 5d and 6s states of PtSA in N_{2C} site are located above the Fermi level (**Fig. 5c and 5d**). This suggests that the 5d and 6s states of PtSA in the C_{2C} site owns a stronger ability to capture the photogenerated electrons than that in the N_{2C} site on the thermodynamics. Especially, the 5d states of PtSA in the C_{2C} site can greatly contribute to the reduction of adsorbed proton (H⁺).^[6,30] As for the PtNP, its 5d and 6s states contain the distribution features of PtSAs in C_{2C} and N_{2C} sites due to the simultaneous formation of Pt-C and Pt-N bonds (**Fig. 5e and 5f**).

Two photogenerated electrons were added into the above models to further explore the electron transfer between *g*-C₃N₄ and PtSA. The results show that an obvious electron transfer occurs between PtSA and neighbor C_{2C} site (**Fig. 5g**). As a result, the PtSA traps the additional electrons (skyblue region in **Fig. 5g**). However, the PtSA in N_{2C} sites only show a localized symmetrical electron redistribution, which cannot contribute to the effective electron transfer from *g*-C₃N₄ to PtSA (**Fig. 5h**). This is considered from the reason that the C atom has a smaller electronegativity than the N atom. Thus the C_{2C} atom is easier to provide PtSA with photogenerated electrons than the N_{2C} atom. For the PtNP, no remarkable electron aggregation is observed because the additional electrons are dispersed in the whole PtNP (**Fig. 5i**). According to above simulations, it is suggested that the formation of Pt-C_{2C} structure by RMSI greatly enhance the photogenerated electron-captured ability of PtSA.

We further investigated the reaction energy of H⁺ adsorption and H₂ desorption on PtSAs in C_{2C}, N_{2C} sites and PtNP, which are the two important steps in the photocatalytic H₂ production.^[31-34] The results show that the adsorptions of two H⁺ ions on PtSAs in C_{2C}, N_{2C} sites and PtNP are all easy to occur in thermodynamics, corresponding to the negative adsorption energies (E_{ads}) of -6.97, -7.63 and -9.09 eV, respectively. However, the difference is that the desorption energy (E_{des}) of H₂ on the PtSA-C_{2C} site is fairly smaller than that on the PtSA in N_{2C} site or PtNP (**Fig. 5j-l and S11**). Thus the formation of H₂ on the PtSA in C_{2C} site is easier than that on the PtSA in N_{2C} site or PtNP. The low E_{des} on PtSA in C_{2C} site can be attributed to two reasons: the high proton-reduced degree and the

short distance between two adsorbed H atoms. However, the low electron density of PtSA in N_{2C} site decreases the proton-reduced degree, which inhibits the breaking of Pt-H bond. On the PtNP surface, the two H atoms are located at two different Pt sites. The long Pt-Pt bond limits the recombination of two adsorbed H atoms. Hence, the PtSA in C_{2C} site has an optimized H₂-production ability compared to the PtSA-N_{2C} or PtNP sites due to the electronic and geometric effects caused by the RMSI.

4. Conclusions

To summarize, we demonstrate a strong RMSI between PtSA and electron-deficient *g*-C₃N₄ achieved by a new *in-situ* photocatalytic reduction method at a sub-zero temperature. The rich N vacancies in *g*-C₃N₄ are significant for the construction of the RMSI. The RMSI can not only improve the stability of supported PtSA by the strong Pt-C_{2C} bonds, but also enhance the performances of PtSA for capturing electron and evolving H₂ *via* the electronic and geometric effects. As a result, the RMSI contributes to the supra-high-density PtSAs (0.35 mg m⁻²) on the electron-deficient *g*-C₃N₄, which shows an enhanced photocatalytic H₂-production activity. This study not only provides a new method to build a RMSI between metal and non-oxide-based support at a sub-zero temperature, but also guide the preparation, stability and electronic optimization of high-density supported single atom catalysts.

Acknowledgement

The authors are grateful for the financial supports of this work from the National Natural Science Foundation of China (Grant No. 51671003), the National Basic Research Program of China (Grant No. 2016YFB0100201) and start-up support from Peking University and the Young Thousand Talented Program. The authors would like to thank NSRL, BSRF, and SSRF for the synchrotron beam time. The calculations were performed on the computing system in Jincai Zhao's group of Institute of Chemistry Chinese Academy of Sciences.

References

- [1] J. Kim, C.W. Roh, S.K. Sahoo, S. Yang, J. Bae, J.W. Han, H. Lee, Highly Durable Platinum Single-Atom Alloy Catalyst for Electrochemical Reactions, *Advanced Energy Materials* 8 (2018) DOI: 10.1002/aenm.201701476.
- [2] S. Yang, J. Kim, Y.J. Tak, A. Soon, H. Lee, Single-Atom Catalyst of Platinum Supported on Titanium Nitride for Selective Electrochemical Reactions, *Angewandte Chemie-International Edition* 55 (2016) 2058-2062.
- [3] H.S. Wei, X.Y. Liu, A.Q. Wang, L.L. Zhang, B.T. Qiao, X.F. Yang, Y.Q. Huang, S. Miao, J.Y. Liu, T. Zhang, FeO_x-supported platinum single-atom and pseudo-single-atom catalysts for

chemoselective hydrogenation of functionalized nitroarenes, *Nature Communications* 5 (2014) DOI: 10.1038/ncomms6634.

[4] L. Nie, D.H. Mei, H.F. Xiong, B. Peng, Z.B. Ken, X.I.P. Hernandez, A. DeLariva, M. Wang, M.H. Engelhard, L. Kovarik, A.K. Datye, Y. Wang, Activation of surface lattice oxygen in single-atom Pt/CeO₂ for low-temperature CO oxidation, *Science* 358 (2017) 1419-1423.

[5] H.B. Zhang, P.F. An, W. Zhou, B.Y. Guan, P. Zhang, J.C. Dong, X.W. Lou, Dynamic traction of lattice-confined platinum atoms into mesoporous carbon matrix for hydrogen evolution reaction, *Science Advances* 4 (2018) DOI: 10.1126/sciadv.aao6657.

[6] H.H. Wei, K. Huang, D. Wang, R.Y. Zhang, B.H. Ge, J.Y. Ma, B. Wen, S. Zhang, Q.Y. Li, M. Lei, C. Zhang, J. Irawan, L.M. Liu, H. Wu, Iced photochemical reduction to synthesize atomically dispersed metals by suppressing nanocrystal growth, *Nature Communications* 8 (2017) DOI: 10.1038/s41467-017-01521-4.

[7] P.X. Liu, Y. Zhao, R.X. Qin, S.G. Mo, G.X. Chen, L. Gu, D.M. Chevrier, P. Zhang, Q. Guo, D.D. Zang, B.H. Wu, G. Fu, N.F. Zheng, Photochemical route for synthesizing atomically dispersed palladium catalysts, *Science* 352 (2016) 797-801.

[8] J. Jones, H.F. Xiong, A.T. Delariva, E.J. Peterson, H. Pham, S.R. Challa, G.S. Qi, S. Oh, M.H. Wiebenga, X.I.P. Hernandez, Y. Wang, A.K. Datye, Thermally stable single-atom platinum-on-ceria catalysts via atom trapping, *Science* 353 (2016) 150-154.

[9] T. He, S.M. Chen, B. Ni, Y. Gong, Z. Wu, L. Song, L. Gu, W.P. Hu, X. Wang, Zirconium-Porphyrin-Based Metal-Organic Framework Hollow Nanotubes for Immobilization of Noble-Metal Single Atoms, *Angewandte Chemie-International Edition* 57 (2018) 3493-3498.

[10] T. Simon, M.T. Carlson, J.K. Stolarczyk, J. Feldmann, Electron Transfer Rate vs Recombination Losses in Photocatalytic H₂ Generation on Pt-Decorated CdS Nanorods, *Acs Energy Letters* 1 (2016) 1137-1142.

[11] L.H. Zhang, L.L. Han, H.X. Liu, X.J. Liu, J. Luo, Potential-Cycling Synthesis of Single Platinum Atoms for Efficient Hydrogen Evolution in Neutral Media, *Angewandte Chemie-International Edition* 56 (2017) 13694-13698.

[12] F.F. Schweinberger, M.J. Berr, M. Doblinger, C. Wolff, K.E. Sanwald, A.S. Crampton, C.J. Ridge, F. Jackel, J. Feldmann, M. Tschurl, U. Heiz, Cluster Size Effects in the Photocatalytic Hydrogen Evolution Reaction, *Journal Of the American Chemical Society* 135 (2013) 13262-13265.

[13] N.C. Cheng, S. Stambula, D. Wang, M.N. Banis, J. Liu, A. Riese, B.W. Xiao, R.Y. Li, T.K. Sham, L.M. Liu, G.A. Botton, X.L. Sun, Platinum single-atom and cluster catalysis of the hydrogen evolution reaction, *Nature Communications* 7 (2016) DOI: 10.1038/ncomms13638.

- [14] S. Penner, M. Armbruster, Formation of Intermetallic Compounds by Reactive Metal-Support Interaction: A Frequently Encountered Phenomenon in Catalysis, *Chemcatchem* 7 (2015) 374-392.
- [15] W.E. Wallace, Intermetallic Compounds in Catalysis, *Chemtech* 12 (1982) 752-754.
- [16] K. Murata, Y. Mahara, J. Ohyama, Y. Yamamoto, S. Arai, A. Satsuma, The Metal-Support Interaction Concerning the Particle Size Effect of Pd/Al₂O₃ on Methane Combustion, *Angewandte Chemie-International Edition* 56 (2017) 15993-15997.
- [17] S.Y. Yao, X. Zhang, W. Zhou, R. Gao, W.Q. Xu, Y.F. Ye, L.L. Lin, X.D. Wen, P. Liu, B.B. Chen, E. Crumlin, J.H. Guo, Z.J. Zuo, W.Z. Li, J.L. Xie, L. Lu, C.J. Kiely, L. Gu, C. Shi, J.A. Rodriguez, D. Ma, Atomic-layered Au clusters on alpha-MoC as catalysts for the low-temperature water-gas shift reaction, *Science* 357 (2017) 389-393.
- [18] G.P. Gao, Y. Jiao, E.R. Waclawik, A.J. Du, Single Atom (Pd/Pt) Supported on Graphitic Carbon Nitride as an Efficient Photocatalyst for Visible-Light Reduction of Carbon Dioxide, *Journal Of the American Chemical Society* 138 (2016) 6292-6297.
- [19] L.L. Lin, W. Zhou, R. Gao, S.Y. Yao, X. Zhang, W.Q. Xu, S.J. Zheng, Z. Jiang, Q.L. Yu, Y.W. Li, C. Shi, X.D. Wen, D. Ma, Low-temperature hydrogen production from water and methanol using Pt/alpha-MoC catalysts, *Nature* 544 (2017) 80-83.
- [20] W. Liu, L.L. Cao, W.R. Cheng, Y.J. Cao, X.K. Liu, W. Zhang, X.L. Mou, L.L. Jin, X.S. Zheng, W. Che, Q.H. Liu, T. Yao, S.Q. Wei, Single-Site Active Cobalt-Based Photocatalyst with a Long Carrier Lifetime for Spontaneous Overall Water Splitting, *Angewandte Chemie-International Edition* 56 (2017) 9312-9317.
- [21] J.P. Perdew, Y. Wang, Accurate and Simple Analytic Representation of the Electron-Gas Correlation-Energy, *Physical Review B* 45 (1992) 13244-13249.
- [22] J.P. Perdew, K. Burke, M. Ernzerhof, Generalized gradient approximation made simple, *Physical Review Letters* 77 (1996) 3865-3868.
- [23] Y.Y. Kang, Y.Q. Yang, L.C. Yin, X.D. Kang, G. Liu, H.M. Cheng, An Amorphous Carbon Nitride Photocatalyst with Greatly Extended Visible-Light-Responsive Range for Photocatalytic Hydrogen Generation, *Advanced Materials* 27 (2015) 4572-4577.
- [24] Y.Y. Kang, Y.Q. Yang, L.C. Yin, X.D. Kang, L.Z. Wang, G. Liu, H.M. Cheng, Selective Breaking of Hydrogen Bonds of Layered Carbon Nitride for Visible Light Photocatalysis, *Advanced Materials* 28 (2016) 6471-6477.
- [25] W.G. Tu, Y. Xu, J.J. Wang, B.W. Zhang, T.H. Zhou, S.M. Yin, S.Y. Wu, C.M. Li, Y.Z. Huang, Y. Zhou, Z.G. Zou, J. Robertson, M. Kraft, R. Xu, Investigating the Role of Tunable Nitrogen Vacancies in Graphitic Carbon Nitride Nanosheets for Efficient Visible-Light-Driven H₂ Evolution and CO₂ Reduction, *Acs Sustainable Chemistry & Engineering* 5 (2017) 7260-7268.

- [26] X.G. Li, W.T. Bi, L. Zhang, S. Tao, W.S. Chu, Q. Zhang, Y. Luo, C.Z. Wu, Y. Xie, Single-Atom Pt as Co-Catalyst for Enhanced Photocatalytic H₂ Evolution, *Advanced Materials* 28 (2016) 2427-2431.
- [27] H.H. Ou, L.H. Lin, Y. Zheng, P.J. Yang, Y.X. Fang, X.C. Wang, Tri-s-triazine-Based Crystalline Carbon Nitride Nanosheets for an Improved Hydrogen Evolution, *Advanced Materials* 29 (2017) DOI: 10.1002/adma.201700008.
- [28] W. Che, W.R. Cheng, T. Yao, F.M. Tang, W. Liu, H. Su, Y.Y. Huang, Q.H. Liu, J.K. Liu, F.C. Hu, Z.Y. Pan, Z.H. Sun, S.Q. Wei, Fast Photoelectron Transfer in (C-ring)-C₃N₄ Plane Heterostructural Nanosheets for Overall Water Splitting, *Journal Of the American Chemical Society* 139 (2017) 3021-3026.
- [29] S.B. Wang, B.Y. Guan, X.W.D. Lou, Construction of ZnIn₂S₄-In₂O₃ Hierarchical Tubular Heterostructures for Efficient CO₂ Photoreduction, *Journal Of the American Chemical Society* 140 (2018) 5037-5040.
- [30] X. Cheng, Y.H. Li, L.R. Zheng, Y. Yan, Y.F. Zhang, G. Chen, S.R. Sun, J.J. Zhang, Highly active, stable oxidized platinum clusters as electrocatalysts for the hydrogen evolution reaction, *Energy & Environmental Science* 10 (2017) 2450-2458.
- [31] E. Skulason, V. Tripkovic, M.E. Bjorketun, S. Gudmundsdottir, G. Karlberg, J. Rossmeisl, T. Bligaard, H. Jonsson, J.K. Norskov, Modeling the Electrochemical Hydrogen Oxidation and Evolution Reactions on the Basis of Density Functional Theory Calculations, *Journal Of Physical Chemistry C* 114 (2010) 22374-22374.
- [32] P.T. Wang, X. Zhang, J. Zhang, S. Wan, S.J. Guo, G. Lu, J.L. Yao, X.Q. Huang, Precise tuning in platinum-nickel/nickel sulfide interface nanowires for synergistic hydrogen evolution catalysis, *Nature Communications* 8 (2017) DOI: 10.1038/ncomms14580.
- [33] J.R. Feng, F. Lv, W.Y. Zhang, P.H. Li, K. Wang, C. Yang, B. Wang, Y. Yang, J.H. Zhou, F. Lin, G.C. Wang, S.J. Guo, Iridium-Based Multimetallic Porous Hollow Nanocrystals for Efficient Overall-Water-Splitting Catalysis, *Advanced Materials* 29 (2017) DOI: 10.1002/adma.201703798.
- [34] J.P. Lai, S.P. Li, F.X. Wu, M. Saqib, R. Luque, G.B. Xu, Unprecedented metal-free 3D porous carbonaceous electrodes for full water splitting, *Energy & Environmental Science* 9 (2016) 1210-1214.

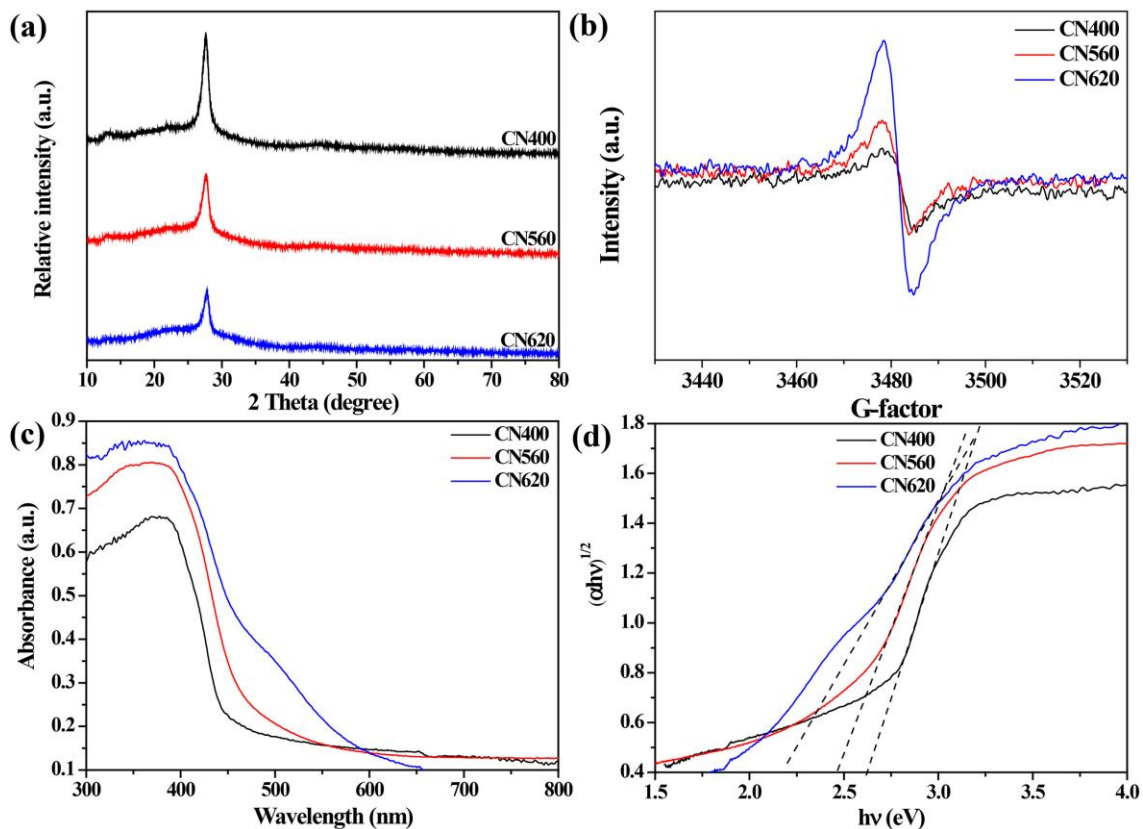
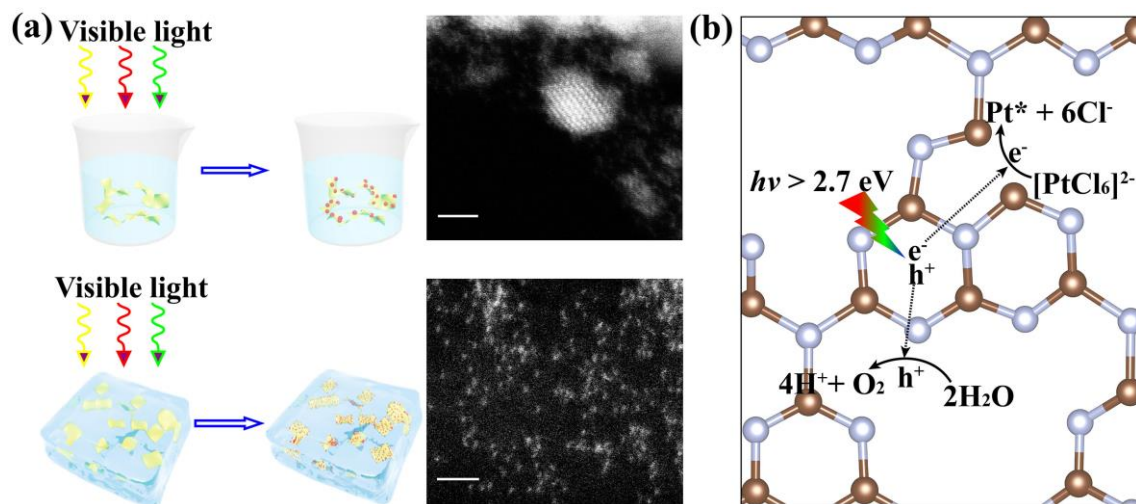


Fig. 1. Physical characterization of CN400, CN560 and CN620. (a) XRD, (b) ESR and (c, d) DRS patterns. XRD patterns of all prepared sample are assigned to g - C_3N_4 . The band gaps of CN400, CN560 and CN620 are calculated to be 2.63, 2.46 and 2.17 eV, respectively.



Scheme 1. Schematic illustration of the icing-assisted *in-situ* photocatalytic reduction method for preparing the supra-high-density PtSAs-loaded $g\text{-C}_3\text{N}_4$. In a typical photocatalytic reduction of H_2PtCl_6 on $g\text{-C}_3\text{N}_4$ photocatalyst, the adsorbed $[\text{PtCl}_6]^{2-}$ was reduced into metal Pt species by the photogenerated electrons from the light excitation of $g\text{-C}_3\text{N}_4$. The PtNP was directly obtained by the diffusion and nucleation of metal Pt species on the surface of $g\text{-C}_3\text{N}_4$. However, under the icing assistance, only the surface adsorbed $[\text{PtCl}_6]^{2-}$ at the N vacancies could be *in-situ* reduced into the PtSAs without aggregation. Scale bar: 2 nm.

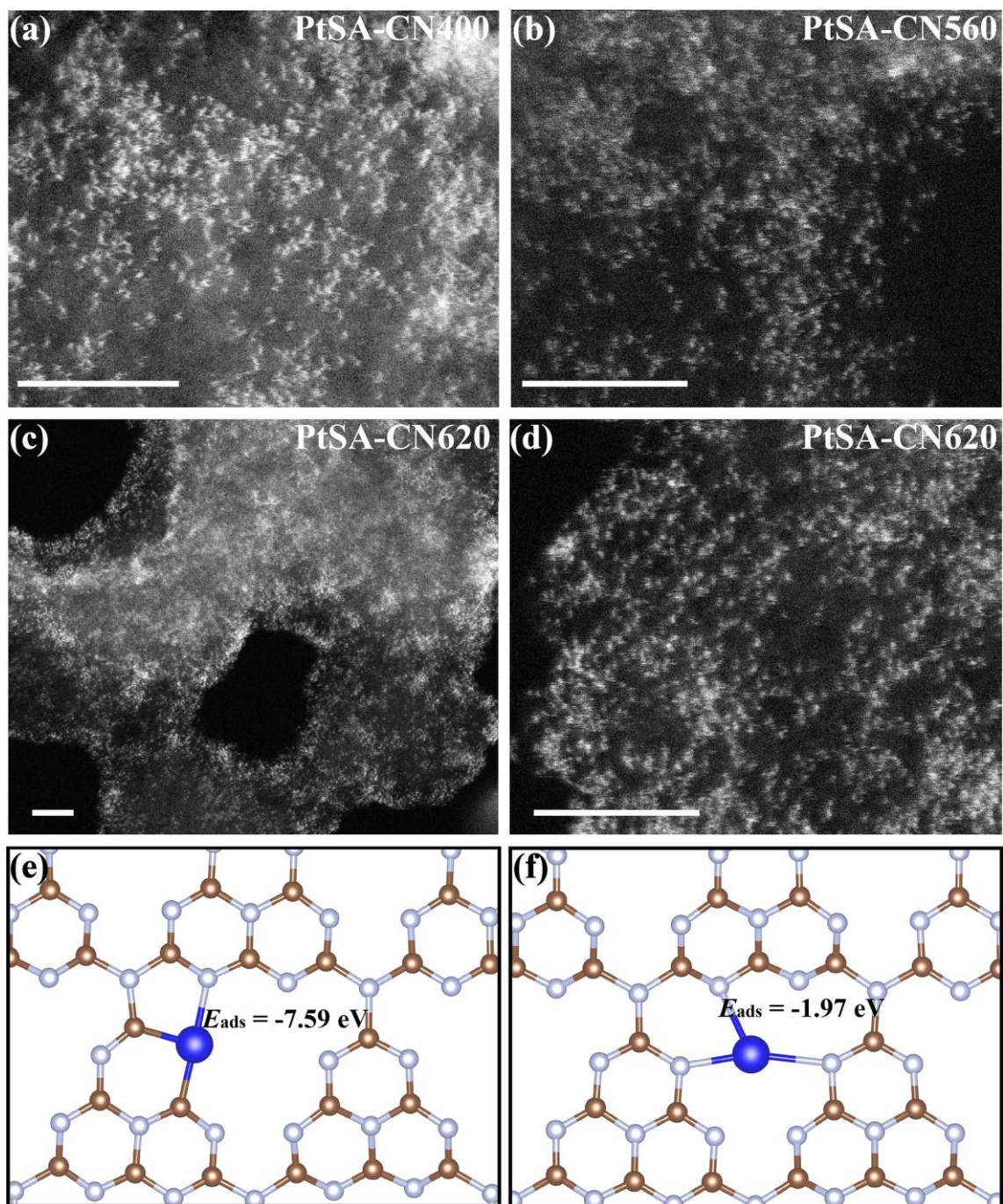


Fig. 2. HAADF-STEM images of (a) PtSA-CN400, (b) PtSA-CN560 and (c, d) PtSA-CN620. The geometry structures of PtSA-trapped at the (e) C₂C and (f) N₂C sites. Scale bar: 5 nm.

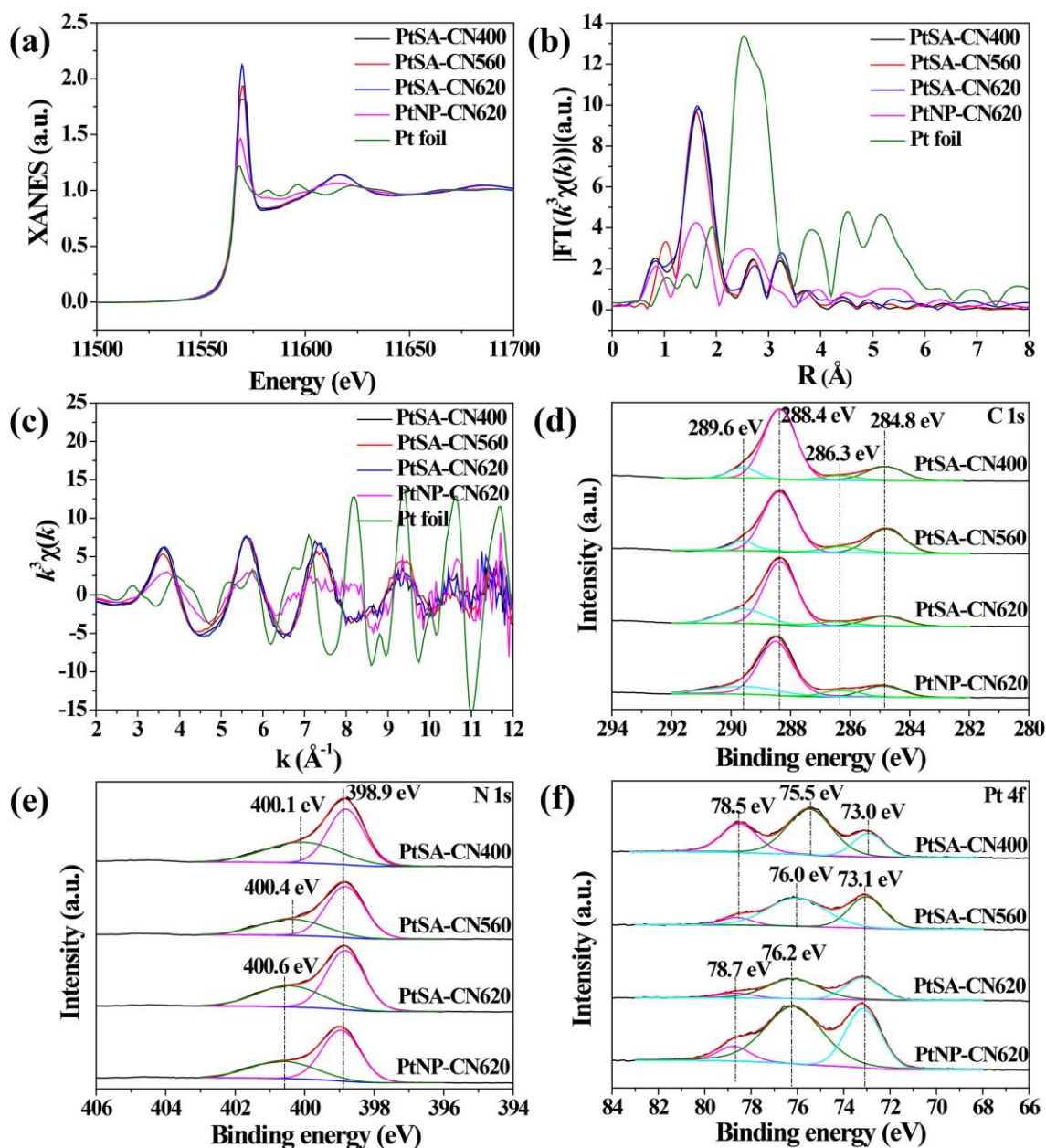


Fig. 3. (a) Pt L₃-edge XANES spectra and the corresponding k³-weighted FT spectra at (b) R space and (c) k space. XPS survey spectra of (d) C 1s, (e) N 1s and (f) Pt 4f in PtSA-CN400, PtSA-CN560, PtSA-CN620 and PtNP-CN620.

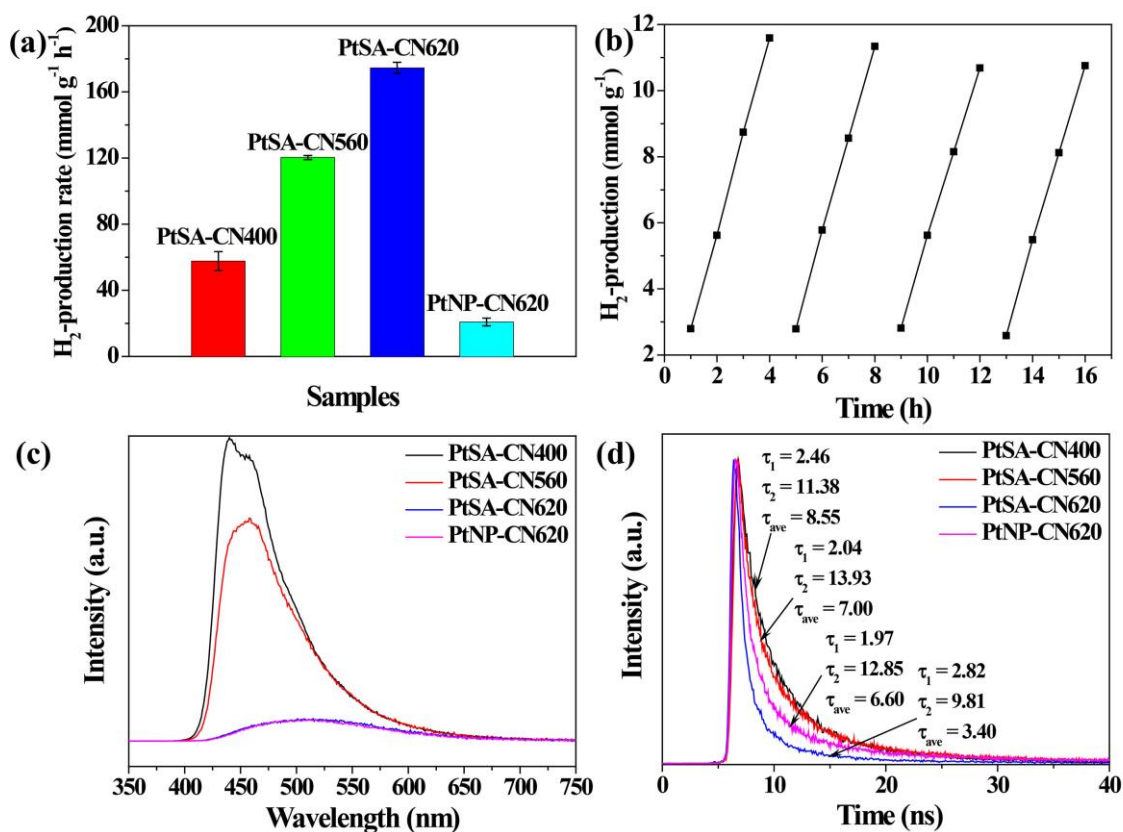


Fig. 4. (a) The H₂ production rates of PtSA-CN400, PtSA-CN560, PtSA-CN620 and PtNP-CN620 normalized to the mass of Pt cocatalyst and (d) the cycling H₂ production activity of PtSA-CN620. All H₂ production experiments used triethanolamine as the sacrifice agent. The H₂ production rates were tested under visible light (> 420 nm) irradiation.

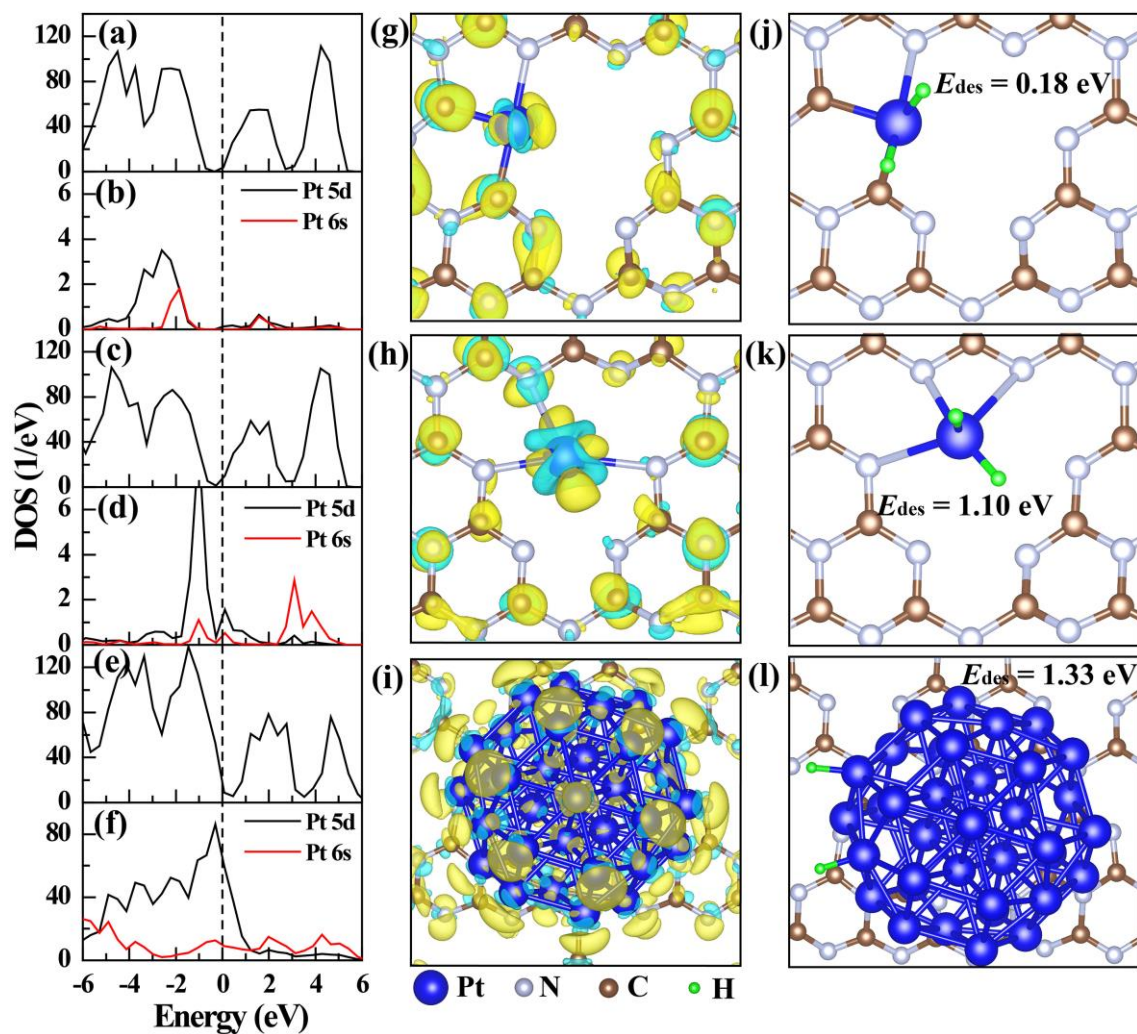


Fig. 5. The geometry structure and electronic properties. The projected density of state (PDOS) plots of PtSA-CN with PtSA at the (a and b) C_{2C} and (c and d) N_{2C} sites and (e and f) PtNP- C_3N_4 . And (g-i) the corresponding charge density difference maps. The H_2 desorption on PtSA at the (j) C_{2C} and (k) N_{2C} sites and (l) PtNP- C_3N_4 . The skyblue and yellow isosurfaces stand for the negative charge and positive charge, respectively. The isosurface of charge density is $0.005 \text{ e} \text{ \AA}^{-3}$ for all figures. The dashed line stands for the Fermi level. The H_2 desorption on other surface sites in PtNP is shown in **Fig. S9**.